Contributions to Mineralogy and Petrology (2021) 176:27
https://doi.org/10.1007/s00410-021-01786-5

ORIGINAL PAPER

Corundum-quartz metastability: the influence of a nanometer-sized phase on mineral equilibria in the system Al_2O_3–SiO_2–H_2O

Dina S. Schultze[1,2] · Richard Wirth[3] · Bernd Wunder[3] · Anselm Loges[1,2] · Max Wilke[4] · Gerhard Franz[2]

Received: 10 October 2020 / Accepted: 28 February 2021 / Published online: 23 March 2021

Abstract

The metastable paragenesis of corundum and quartz is rare in nature but common in laboratory experiments where according to thermodynamic predictions aluminum–silicate polymorphs should form. We demonstrate here that the existence of a hydrous, silicon-bearing, nanometer-thick layer (called "HSNL") on the corundum surface can explain this metastability in experimental studies without invoking unspecific kinetic inhibition. We investigated experimentally formed corundum reaction products synthesized during hydrothermal and piston–cylinder experiments at 500–800 °C and 0.25–1.8 GPa and found that this HSNL formed inside and on the corundum crystals, thereby controlling the growth behavior of its host. The HSNL represents a substitution of Al with Si and H along the basal plane of corundum. Along the interface of corundum and quartz, the HSNL effectively isolates the bulk phases corundum and quartz from each other, thus apparently preventing their reaction to the stable aluminum silicate. High temperatures and prolonged experimental duration lead to recrystallization of corundum including the HSNL and to the formation of quartz + fluid inclusions inside the host crystal. This process reduces the phase boundary area between the bulk phases, thereby providing further opportunity to expand their coexistence. In addition to its small size, its transient nature makes it difficult to detect the HSNL in experiments and even more so in natural samples. Our findings emphasize the potential impact of nanometer-sized phases on geochemical reaction pathways and kinetics under metamorphic conditions in one of the most important chemical systems of the Earth's crust.

Keywords Experimental · Metastability · Corundum · Quartz · Nanolayers · Aluminium–silicates

Introduction

The system Al_2O_3–SiO_2–H_2O (ASH) is one of the most important and widely studied chemical systems in geosciences and material sciences. Because SiO_2 and Al_2O_3 are the most abundant chemical components in the Earth's crust (Rudnick and Gao 2003) and H_2O is nearly ubiquitous on the Earth's surface, the minerals formed by these components feature prominently in many crustal rocks. Understanding the geological and mineralogical processes shaping the Earth's crust hence depends on comprehensive knowledge of this seemingly simple system. Extensive experimentation has been conducted since the beginning of the twentieth century to determine phase relations in and thermodynamic properties of the system (e.g. Kerrick 1990; Schneider and Komarneni 2005). Due to their importance as geothermobarometers in natural rocks, the synthesis of the Al_2SiO_5 polymorphs (andalusite, sillimanite, kyanite) and the determination of their common invariant point has been the scope of numerous studies (e.g. Althaus 1966; Holdaway 1971; Pattison 1992). Despite their commonness in metamorphic rocks, the Al_2SiO_5 polymorphs are notoriously difficult to synthesize without using natural seeds and the metamorphic transformations between the polymorphs are sluggish (Harlov and Milke 2002; Kihle et al. 2010), which impedes the precise determination of the univariant

Communicated by Timothy L. Grove.

✉ Dina S. Schultze
dina.schultze@web.de

[1] Abteilung Mineralogie, Freie Universität Berlin, Malteserstr. 74-100, 12249 Berlin, Germany

[2] Fachgebiet Angewandte Geochemie, Technische Universität Berlin, Ernst-Reuter-Platz 1, 10587 Berlin, Germany

[3] Deutsches GeoForschungs Zentrum Potsdam, Telegrafenberg, 14473 Potsdam, Germany

[4] Institut für Erd-und Umweltwissenschaften, Universität Potsdam, Karl-Liebknecht-Str. 24-25, 14476 Potsdam-Golm, Germany

curves. In addition, the reaction pathway of the formation reaction: $Al_2O_3 + SiO_2 \rightarrow Al_2SiO_5$ appears to be obstructed (Harlov et al. 2008). Corundum and quartz do not react towards Al_2SiO_5 polymorphs at experimental temperatures and pressures relevant for comparison with most natural samples even if the reaction is promoted by additional fluid, and instead form a very persistent metastable assemblage. This is why most experimental studies use other starting materials, such as amorphous Al_2O_3 and SiO_2, hydroxides, gels or glasses (e.g. Carr and Fyfe 1960; Aramaki and Roy 1963). Harlov and Milke (2002) produced kyanite from a natural quartz + corundum mixture, but only at 1200 °C and 2 GPa and with the addition of water. However, even if the aforementioned different starting materials are used, corundum and quartz are frequently produced inside the stability fields of andalusite, sillimanite, or kyanite, (see Fig. 1a, yellow). Mullite, the high temperature, impact, or contact metamorphism-related aluminium silicate is frequently found in experiments where sillimanite should be stable (Fig. 1a, red) and often occurs in association with corundum and quartz or cristobalite (Fig. 1a, orange) (Aramaki and Roy 1962; Bratton and Brindley 1962; Brearley and Rubie 1990). The metastable mullite occurrence is mostly restricted to experiments with pressures below 0.1 GPa, whereas corundum and quartz occur within a pressure range of 0.1 MPa–0.8 GPa and temperatures of 420–2000 °C, with most metastable assemblages being reported below 0.3 GPa and 1300 °C (Clark et al. 1957; Carr and Fyfe 1960; Giardini et al. 1961; Wahl et al. 1961; Aramaki and Roy 1963; DeVries 1964; Day 1973; Huang and Wyllie 1974; Saalfeld and Junge 1983; Grapes 2011). An explanation for the broadly observed experimental metastability has not been found. This is troubling since the interpretation of natural samples and thermodynamic modelling in the ASH system relies on experimental data that are affected by this phenomenon. The fact that the experiments (Fig. 1a) all seemingly disobey the laws of thermodynamics by producing corundum and quartz emphasizes the need for a better understanding of this problem. We will show here that the formation of the thermodynamically stable phase is inhibited by the formation of a nanometer-sized phase, which effectively separates the metastable phases and hampers achievement of thermodynamic equilibrium.

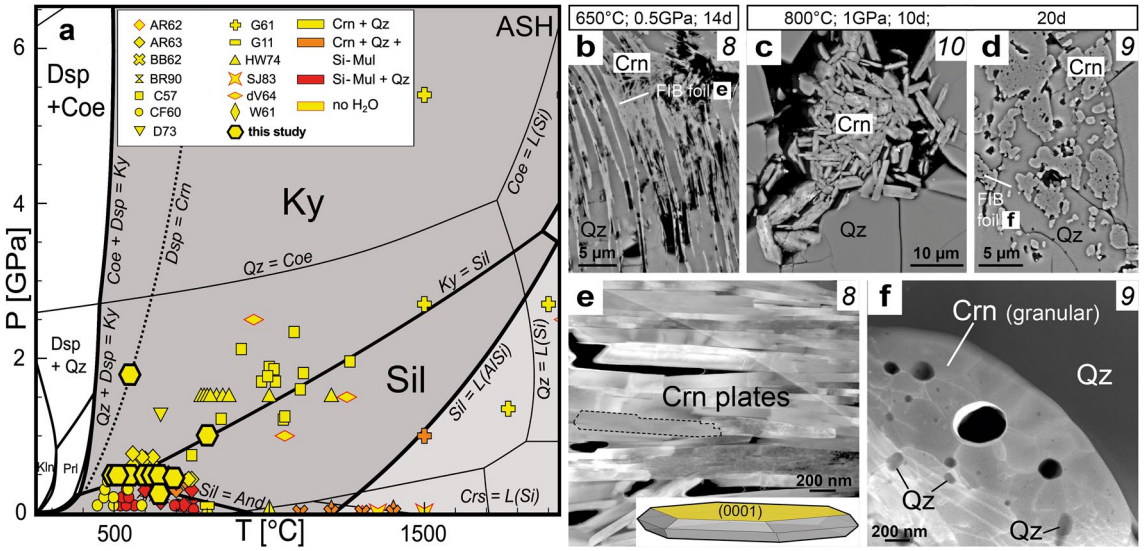

Fig. 1 Examples for metastable formation of corundum (Crn) and quartz (Qz) in experiments: **a** petrogenetic grid of the system Al_2O_3–SiO_2–H_2O (ASH) produced with the program Perplex_X (Connolly 2009), using the thermodynamic dataset of Holland and Powell (2011), mineral abbreviations after Whitney and Evans (2010) and Holland and Powell (2011). Indicated are experiments that yielded metastable Qz + Crn (yellow), Qz + Si rich mullite (Si–Mul) (red), and Qz + Crn + Si–Mul (orange) [from this study; Clark et al. 1957 (C57); Carr and Fyfe 1960 (CF60); Giardini et al. 1961 (G61); Wahl et al. 1961 (W61); Aramaki and Roy 1962 (AR62); Bratton and Brindley 1962 (BB62); Aramaki and Roy 1963 (AR63); DeVries 1964 (dV64); Day 1973 (D73); Huang and Wyllie 1974 (HW74); Saalfeld and Junge 1983 (SJ83); Brearley and Rubie 1990 (BR90); Grapes 2011 (G11), a summary of the data is given in Online Resource 6]. **b–d** BSE images (EMP) of Crn + Qz produced in experiments of this study (experimental run numbers are indicated in italic, see Table 1) with increasing temperature (*T*), pressure (*P*) and experiment duration (*t*) from left to right. Note increasing width in [0001] direction of the Crn plates with increasing *T* and *t*, and the change of crystal habit from 650 to 800 °C from flat prism after 10 days to porous granular Crn grains after 20 days. **e**, **f** Detail-transmission electron microscopy (TEM) images taken of FIB foils indicated in (**b**) and (**d**), respectively. **e** Bright field image of an accumulation of flat Crn plates at 650 °C (including crystal model). **f** High angle annular dark field (HAADF) image of granular Crn with multiple sub-grain boundaries at 800 °C; 20 days in contact with Qz and including Qz-fluid inclusions

Experiments and methods

A series of experiments listed in Table 1 was conducted using piston–cylinder apparatuses ($P > 0.5$ GPa) and cold seal pressure vessels ($P \leq 0.5$ GPa) and different sources of silica (quartz, amorphous SiO_2, pyrophyllite) as well as alumina (corundum, γ-Al_2O_3, diaspore, pyrophyllite) with the aim of testing the persistence of corundum-quartz metastability in the stability fields of all three aluminim silicate polymorphs. To assure sufficiently high reaction rates, all experiments were H_2O-bearing, which was either added as deionized water or liberated by dehydrating diaspore or pyrophyllite during the experiments. All experiments were silica saturated with respect to quartz, and thus the silica and alumina reactants should only produce the Al_2SiO_5 polymorphs and quartz as solid products in equilibrium at given *P*–*T*, but no corundum. Additionally, in order to overcome the activation energy necessary for Al_2SiO_5 nucleation from the fluid phase, different cooling or decompression pathways were included in some of the experiments (Beitter et al. 2008, Table 1).

Starting materials

Amorphous SiO_2 powder with 0.5 µm grain size (Alfa Aesar) was used as silica source in most experiments. The powder was analyzed with XRD (X-ray diffractometry) to exclude the presence of minor crystalline components. Natural inclusion-free quartz grains (< 30 µm) were used in run 5 (Table 1). Amorphous γ-Al_2O_3 (Alfa Aesar) was used as main aluminum source, which was also analyzed with XRD. Natural and synthetic corundum single crystals were used in some experiments to monitor the reaction of preexisting corundum with quartz or SiO_2 saturated fluid along the crystals surface. Trace element-free Czochralski grown synthetic corundum (Table 2), obtained from Crystal GmbH Berlin, consisted of 1 × 10 × 10 mm chips, with polished basal planes, which allowed for a better crystallographic orientation during preparation of the experimental products and during analyses. The chips were cut into 1 × 1 × 2 mm blocks. Natural gem quality yellow corundum from Sri Lanka was crushed to < 1.5 mm grain size and hand-picked for the experiments to avoid inclusions. Besides small amounts of Fe (0.05 wt% Fe_2O_3), other trace elements are below detection limit (~ 50 ppm) in microprobe analyses of natural corundum (Table 2). Natural diaspore with traces of Fe (Table 2) was used in runs 2, 5, and 9 (Table 1). Pyrophyllite from North Carolina (USA) with trace contents of Fe and Mg (Table 2) was used in run 8.

Experimental setups

Hydrothermal experiments

Experiments ≤ 0.5 GPa were conducted in externally heated cold-seal vessels using water as pressure medium at Technische Universität Berlin. The accuracy of the setup is ± 10 °C for temperature and ± 10 MPa for pressure. Gold capsules were loaded with the starting materials and fluid (Tables 1 and 2); the capsules were then welded, and impermeability was controlled by checking for weight loss after heating the capsules to 100 °C for half an hour.

Table 1 Experiments on the persistency of metastable corundum + quartz formation at Al_2SiO_5 stability conditions

Run number	Starting materials [mg]	H_2O [mg]	*P* [GPa]	*T* [°C]	*t* [d]	Products
1	0.84 (1), 17.92 (4)	17.80	0.5	500 → 490 → 480	5 → 5 → 14	Qz, AlOH
2	2.63 (2), 2.71 (3), 17.42 (4)	–	1.8 → 0.5	550	1 → 7	Qz, Crn
3	1.03 (1), 3.37 (4)	17.60	0.5	600 → 550 → 500	13 → 1 → 1	Qz, Prl, Crn, (AlOH)
4	1.01 (1), 3.57 (4)	17.41	0.5	650 → 636 → 625 → 615	7 → 1 → 0.5 → 0.5	Qz, Crn
5	8.40 (3), 27.31 (5)	20.25	0.5	650 → 636 → 625 → 615	7 → 1 → 0.5 → 0.5	Qz, Crn
6	1.66 (1), 4.03 (2), 3.24 (4)	13.09	0.5	650 → 550	5 → 7	Qz, Crn
7	12.54 (1), 31.96 (4)	38.15	0.45 → 0.25	650	14 → 14	Qz, Crn
8	10.3 (2), 55.99 (6)	–	0.5	650	14	Qz, Crn, Si–Mul
9	13.82 (3), 20.39 (4)	–	1	800	20	Qz, Crn
10	6.24 (2), 23.16 (4)	2.94	1	800	10	Qz, Crn

Starting materials: amorphous γ-Al_2O_3 (1), corundum single crystals (2), diaspore (3), amorphous SiO_2 (4), natural quartz (5), pyrophyllite (6), added deionized water is given in column "H_2O"

Hydrothermal experiments were conducted up to 650 °C; 0.5 GPa, piston–cylinder experiments > 0.5 GPa. Decompression and cooling paths (stepwise) are indicated with arrows in "*P*", "*T*", and "*t*"

Products: *Qz* quartz, *Crn* corundum, *Si–Mul* Si-rich Mullite, *Prl* pyrophyllite, *AlOH* aluminumhydroxide

Table 2 Composition of crystalline experimental starting material; corundum, diaspore, and pyrophyllite

Corundum	Synthetic	Natural	DL
SiO_2	0.06	0.09	25
Al_2O_3	99.94	99.95	50
Fe_2O_3	b.d.	0.05	60
Total	100.00	100.09	–
Pyrophyllite (natural)		DL	
SiO_2	66.82	96	
Al_2O_3	28.10	93	
Fe_2O_3	0.07	195	
MgO	0.03	70	
Total	95.03	–	
Diaspore (natural)		DL	
SiO_2	0.03	83	
TiO_2	0.03	148	
Al_2O_3	83.86	93	
Fe_2O_3	0.70	190	
Total	84.62	–	

WDS results EMP in oxide wt%, detection limits "DL" in element wt ppm

Piston–cylinder press

Gold or platinum capsules were loaded with amorphous silica powder embedding corundum or diaspore grains and/or water, welded, and checked for weight loss after heating (see "Hydrothermal experiments"). The high-pressure assemblies consisted of single or double capsule arrangements, described in detail by Schilling and Wunder (2004). A first assembly with CaF_2 as pressure medium (40 mm length, 22 mm in diameter) was used to conduct run 10 (Table 1), in a graphite furnace, with a Ni–CrNi thermocouple. The thermocouple was in the top position in this assembly, similar to assembly six in Schilling and Wunder (2004). Due to the top-position of the thermocouple, the temperature accuracy is about ± 20 °C, and a temperature gradient of ~ 30 °C is expected (Schilling and Wunder 2004). We applied a pressure correction of 10% to lower pressure due to friction, which was determined afore by calibration experiments on the reaction quartz—coesite. Runs 2 and 9 were conducted in a double-capsule (each 10 mm in length, 3 mm in diameter) CaF_2 assembly (dimensions as in the first assembly), in a graphite furnace, using a Ni–CrNi thermocouple. The design is similar to assembly five of Schilling and Wunder (2004). The thermocouple is positioned between the two capsules. The accuracy is ± 10 °C and the T-gradient is about 10 °C.

Analytical methods

After quenching, the capsules of both hydrothermal and piston cylinder experiments were again checked for weight loss; most capsules were then opened and dried, and some were kept close until thin section production, in order to preserve internal structures. A portion of the products was ground and analyzed for phase identification with powder XRD. XRD analyses were carried out at the Technische Universität Berlin with a Bruker D2 Phaser in a range of 5–80° 2θ, and 0.01° step width per 0.4 s, at 30 kV; 10 mA, using a Cu-anode. A separate portion of the products from hydrothermal experiments was used for 3D-imaging of fine-grained crystals and growth textures on larger corundum grains using a Hitachi S-520 scanning electron microscope (SEM) at Technische Universität Berlin. The samples were gold coated and analyzed at scanning conditions of 15–20 kV acceleration voltage and 10–20 nA beam current. Thin sections were produced from both hydrothermal and piston–cylinder experimental products, by embedding portions of the loose products or the entire capsules in epoxy and polishing to a desirable level. The thin sections were then analyzed with electron microprobe (EMP). EMP analyses of polished and carbon-coated thin sections were conducted using a

JEOL JXA-8530F field emission microprobe at Technische Universität Berlin. Backscattered and secondary electron images as well as wavelength-dispersive X-ray spectroscopy (WDX) analyses were done at scanning conditions of 20 kV and beam currents of 20 nA. Standardization of WDX results was done using Astimex® mineral standards. For transmission electron microscopy (TEM), approximately 15 × 7 × 0.15 µm large foils were cut from the pre-analyzed thin sections by focused ion beam (FIB) milling under ultra-high vacuum conditions using a FEI FIB200 instrument at the GeoForschungsZentrum Potsdam. Placed on a perforated carbon film, the sample foils were analyzed using an electron microscope type FEI Tecnai G2 F20 X-Twin at the GeoForschungsZentrum Potsdam. The TEM was operated at 200 keV with a field emission gun as electron source. High-angle annular dark-field (HAADF) images were acquired as Z-contrast images (camera length 75 mm) or Z-contrast + diffraction contrast images (camera length 220 mm) using a Fishione detector system. Bright- and dark-field images as well as high-resolution lattice fringe images were acquired as energy-filtered images applying a 20-eV window to the primary electron beam. The system used was a Gatan Tridiem energy filter (GIF). Electron energy loss spectra (EELS) were acquired in diffraction mode. Ten spectra were acquired with an acquisition time of 1 s each. Analytical electron microscopy (AEM) was performed with an EDAX X-ray analyser with an ultrathin window. Spectra were acquired in the scanning transmission mode scanning the electron beam within a preselected window, thus minimizing mass loss during electron sputtering. Acquisition time usually was 60 s.

Results

Persistent formation of metastable corundum with variable habit

All experiments ≥ 500 °C produced corundum and quartz (Fig. 1a, Table 1), and in one case additionally mullite. The composition of mullite ranged from slightly Si-enriched 3:2 mullite (molar ratio Al_2O_3:SiO_2) to strongly silica-oversaturated mullite with a composition of $(^{VI}Al_{1.97}Fe_{0.02}Mg_{0.01})_2(^{IV}Al_{2.29}Si_{1.71})O_{9.85}$. Detailed mullite chemistry is given in Online Resource 1, and images of mullite precipitates are given in Online Resource 2 (Supplementary Electronic Material). Quartz grains display equilibrium-growth textures in all piston–cylinder experiments. In hydrothermal experiments with high fluid content, quartz developed euhedral single crystals. Corundum formed in all experiments > 500 °C in direct contact with quartz (Fig. 1b–d). At experimental temperatures of ≤ 500 °C pyrophyllite was found, along with Al-hydroxides and

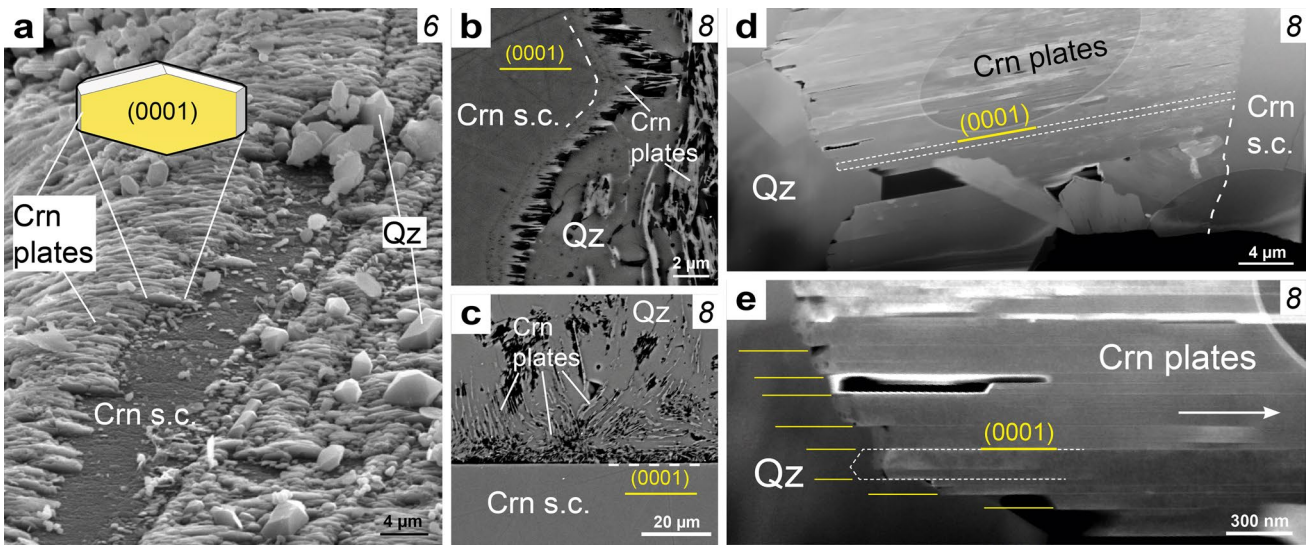

Fig. 2 Corundum single crystals (Crn s.c.) epitactically overgrown by Crn plates: **a** Crn plates grown on preexisting natural Crn single crystal in run 6 (Table 1) forming a Crn plate rim. **b** BSE image of Crn plate rim grown on a surface oblique to (0001) of a synthetic Crn single crystal in run 8. **c** BSE image of the polished (0001) face of the same synthetic Crn grain as in (**d**); no Crn plates are grown on this surface of the single crystal. **d** Overview HAADF image of TEM foil from a crosscut through Crn single crystal (on the right), plate rim with identically oriented but not intergrown Crn plates (middle), and neighboring Qz grain (on the left) from run 8. Crn plates and single crystal are connected along (10–10), and the contact is indicated with a white dashed line. **e** HAADF image of Crn plate–rim [detail of (**d**)] contact with Crn single crystal indicated with a white arrow. The Crn plates are not intergrown with each other along (0001) (grain boundaries indicated in yellow)

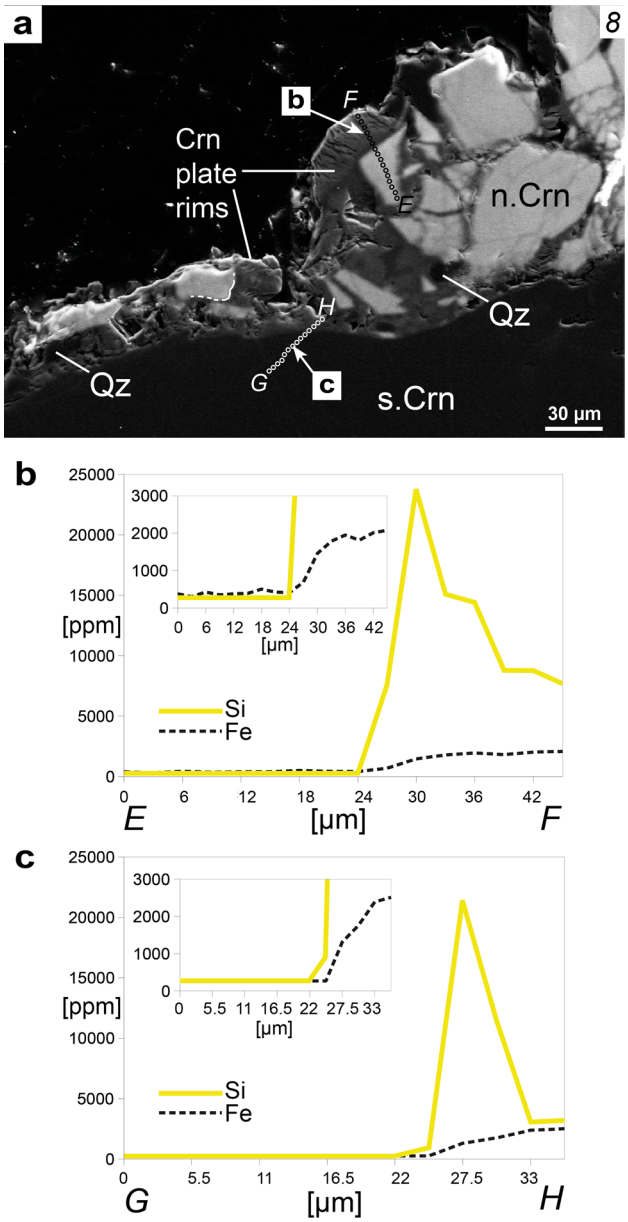

Fig. 3 Thin section of corundum (Crn) single crystals epitactically overgrown by Crn plate rims (run 8): **a** corundum plate rims (gray) around natural "n" (bright gray) and synthetic "s" (dark gray) corundum single crystals in a SEM-CL image. The n.Crn grain is crushed and the shards are connected with Crn plates (gray) and interstitial quartz (Qz) (deep dark gray). Chemical profiles of Si and Fe (EMP data in wt ppm) through n.Crn with corresponding Crn plate rim in (**b**) (*E–F*) and s.Crn and plate rim in (**c**) (*G–H*) are indicated in (**a**). Increased areas of the profiles in (**b**) and (**c**) up to 3000 ppm are included in the profiles. Values of < 260 and < 270 for Si and Fe, respectively, are below detection limit of the EMP analyses. In both (**b**) and (**c**) the Crn plate rim shows highest Si concentrations at the plate rim–single crystal contact (dataset is given in Online Resource 5)

quartz. No Al_2SiO_5 polymorphs were produced in any of the experiments.

Corundum crystallized as flat hexagonal plates or prisms characterized by a large basal pinacoid {0001} and often vanishingly small $\{01\bar{1}2\}$ and $\{0\bar{1}14\}$ faces in most runs, regardless of starting material and experimental setup (see Fig. 1b, c). The faces $\{01\bar{1}2\}$ and $\{0\bar{1}14\}$ could be determined by indexing very thin corundum plates with TEM and comparing the result to the plates' crystal faces. The habit of synthesized corundum displays a strong temperature dependence in that the area (or aspect) ratio of crystal faces $\{0001\}/(\{01\bar{1}2\}+\{0\bar{1}14\})$ decreased with increasing temperature and duration of the experiment (Fig. 1b–d) independent of the alumina starting material (γ-Al_2O_3 or diaspore). At ≥ 600 °C corundum crystallized as flakes or plates with < 200 nm width (Online Resource 3). At 650 °C the corundum crystals reached up to 300 nm in width (Fig. 1b, e), and at 800 °C, up to 5 µm-thick plates or prisms were produced (Fig. 1c, and Online Resource 4).

In experiments using natural and synthetic corundum single crystals (with up to 1 mm diameter) newly formed corundum plates overgrew the crystal surface of the corundum single crystals epitactically with growth directions perpendicular to [0001] forming a corundum plate rim on the single crystals (Fig. 2a–e). However, no corundum plates were found that grew on the polished (0001) faces of the synthetic single crystals (Fig. 2c). Despite the presence of mullite in the matrix of run 8, not a single mullite crystal was found grown on the surface of the corundum single crystals (Figs. 2b, c and 3a). Two element profiles, measured with electron microprobe, through a natural corundum single crystal and associated corundum plate rim (*E–F*) and through a synthetic grain with corresponding plate rim (*G–H*), are presented in Fig. 3b, c, respectively (dataset in Online Resource 5). Both profiles show a pronounced Si maximum with up to 23,000 ppm along the contact of the plate rims with the single crystals. With increasing distance to the contact, Si concentration decreases within the plate rim (Fig. 3b, c). The content of iron in corundum also increases in the rims; however, Fe concentration gradually decreases towards the contact of rim and single crystal, converging to the concentration in the single crystal (Fig. 3b, c). The grain boundary between individual corundum plates in the rims is often less than 5 nm wide (Fig. 2d), but no intergrowth of the plates was observed along (0001) (Fig. 2e), regardless of identical orientation and close vicinity of the neighboring plates in these overgrowth-rims. This indicates that the plates are effectively isolated along their large basal pinacoids (Fig. 2e).

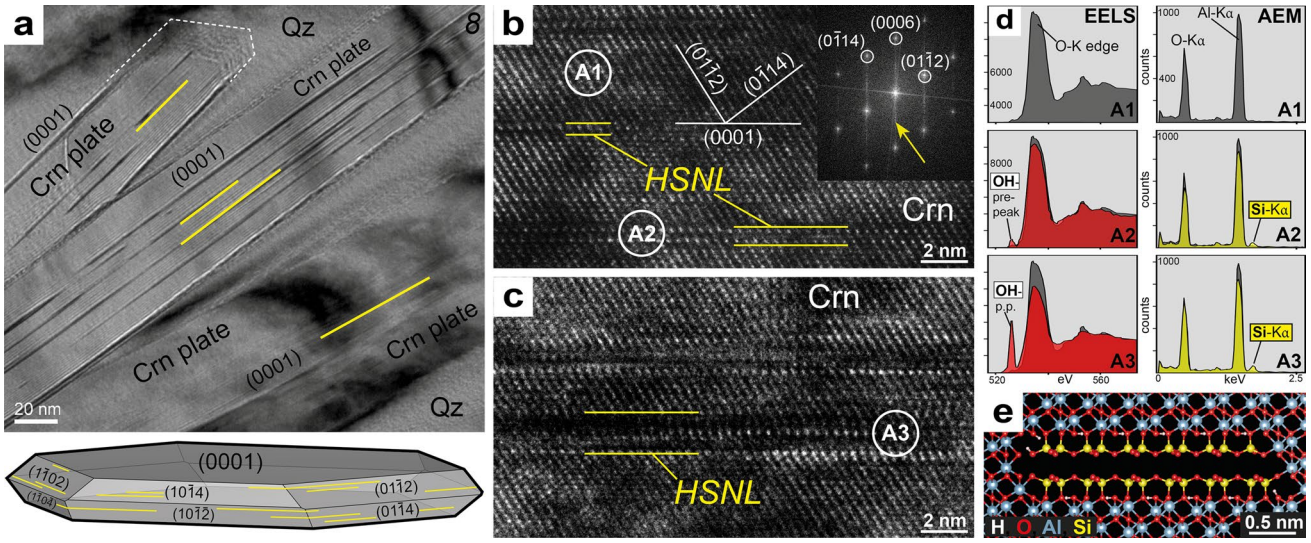

Fig. 4 Transmission electron microscopy (TEM) analyses of corundum (Crn) plates: **a** top: bright field image of four Crn plates (run 8) including hydro-silicate-nanolayers (HSNL) in yellow parallel to (0001), bottom: indexed 3D-crystal model of a Crn plate (created with VESTA, Momma and Izumi 2011). High-resolution transmission electron microscopy (HRTEM) images of double and triple (**b**), and multiple (**c**) HSNLs (yellow) inside Crn. **b** Indexed Crn oriented with {0001} ‖ to the incident beam; note characteristic streak pattern in [0001] (yellow arrow) in electron diffraction image (upper right). **d** TEM-electron energy loss spectroscopy (EELS, left side) and Analytical electron microscopy (AEM, right side) analyses of pure Crn (A1), Crn including triple HSNL (A2), and Crn including multiple HSNL (A3) [analyses spots A1–A3 are indicated in (**b**) and (**c**)]. (A1) is free of OH bonds and Si and hence shows no OH-pre-peak at 528 eV in the EELS spectra (see Wirth and Wunder 2000) and no Si–Kα peak (AEM), (A2) and (A3) with increasing HSNL density OH-pre-peak and Si–Kα peak appear and increase with increasing HSNL density. **e** Model of the proposed molecular structure of a triple HSNL (created with VESTA), where two Si-tetrahedral layers (Si atoms in yellow, oxygen in red) replace three Al-octahedral layers in Crn (Al in blue), the substitution in charge balanced with H^+ (H atoms in white)

Hydro-silicate-nanolayers (HSNL)

TEM investigations showed that synthesized corundum with large basal pinacoids (flake-shaped, plate-shaped corundum and flat prisms, see Fig. 1, Online Resource 3), contains nanometer-sized layers along their basal plane (0001), which represent a systematic disruption of the corundum structure perpendicular to this plane, involving either two (double), three (triple) or multiple Al-octahedral layers (Fig. 4a–c, Online Resource 4). Inside an individual corundum plate the layers expansion along (0001) is limited and double or triple layers can be observed separately (Fig. 4b), whereas along the basal pinacoids of two neighboring, epitactically oriented plates, multiple layers define the entire grain boundary and isolate the plates from each other (Fig. 4c). AEM and EELS analyses were conducted on triple (A2) and multiple (A3) nanolayers as well as on nanolayer free corundum (A1) as a reference (Fig. 4b–d). Within the nanolayers, along $(0001)_{Crn}$ analyses showed that Al is substituted by Si and OH (Fig. 4d). Due to the incorporation of Si and OH, these nanolayers are hereinafter tentatively called hydro-silicate-nanolayers (HSNL, Fig. 4). In electron diffraction images the HSNL within corundum matrix cause a streak pattern in the direction of [0001] (Fig. 4b). The streaking in the diffraction pattern is caused by the very thin layers of HSNL and it is normal to these layers. There is a very weak scattering intensity visible halfway between the (0006) reflections of corundum with a *d*-spacing of approx. 4.32 Å (arrow in Fig. 4b). The d_{hkl} spacing is difficult to measure because the intensity is smeared out and very weak. The *d*-spacing equals approximaltely the distance between two Si-rich layers in Fig. 4e. In order to detect the streak pattern or see double or triple nanolayers in HRTEM mode, the (0001) planes of the analyzed corundum crystal need to be oriented approximately normal to the foil surface and parallel to the electron beam; otherwise, the features are difficult to see or completely hidden (Fig. 4a, Online Resource 4).

The transient nature of HSNL

The influence of experimental pressure on the habit of the corundum crystals seems to be negligible however, at temperatures of 800 °C the duration of the experiments visibly affected the shape of the crystals. While after 10 days the corundum occurred as flat prisms (Fig. 1c), an experiment of 20 days produced granular aggregates of corundum surrounded by and included in quartz (Fig. 1d, f). The longer experiment was part of a series of three experiments with diaspore as Al_2O_3 source. At 550 °C stacks of less than 200 nm-wide corundum plates formed pseudomorphs after

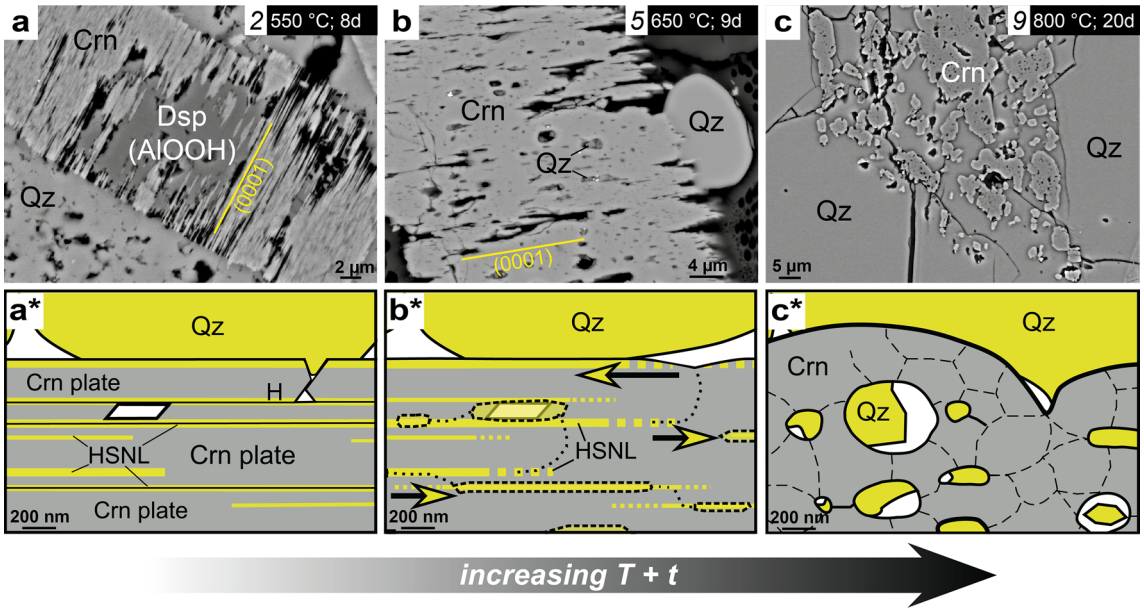

Fig. 5 Series of experiments with diaspore (Dsp) as Al source at different temperatures: **a** stacks of less than 200 nm-wide, parallel Crn plates formed pseudomorph after Dsp in Qz matrix at 550 °C (BSE). **b** Crn plates pseudomorph after Dsp at 650–615 °C, Crn plates are up to 3 µm-thick and contain elongated quartz inclusions inside the plates and between intergrown individuals of the plate stack (BSE). **c** Crn after Dsp at 800 °C is granular and contains round Qz inclusions (BSE). **a*** Interpretive sketch of Crn plates in a Crn-stack pseudomorph after Dsp, as in (**a**). The plates include HSNL inside and along their (0001) surface that is in contact with Qz and likely prevents Crn and Qz from reacting. **b*** Crn plates partly intergrow as a result of the HSNLs being annealed in the Crn stack at higher temperatures, thereby forming thicker Crn plates and elongated Qz inclusions [compare (**b**)]. **c*** At 800 °C the completely recrystallized Crn is composed of numerous sub-grain boundaries and near spherical fluid + Qz inclusions (compare Fig. 1f). The Crn-Qz phase boundary is approximately spherical and the interface between the two phases minimal, which again might prevent the reaction towards Al_2SiO_5

diaspore (Fig. 5a, Table 1). The plates in these stacks are parallel and epitactically aligned, but isolated from one another. At 615–650 °C corundum plates are up to 3 µm-thick, locally inter-grown with adjacent plates in the corundum plate stack, and contain elongated quartz inclusions (Fig. 5b). The former diaspore grain is completely replaced but clearly outlined by the corundum plate stack. At 800 °C and after 20 days, corundum occurred in the aforementioned granular aggregates of up to 50 µm large grains. These are interlocked with quartz, only poorly reflect the former diaspore grain, and contain numerous, often parallel elongated fluid and quartz inclusions (Fig. 5c). Unlike the other two experiments of the series, granular corundum includes no HSNL but, instead, a network of sub-grain boundaries connecting the fluid/solid inclusions (Fig. 1f). Along these sub-grain boundaries, there is an occasional increase in Si, whereas the rest of the grain is Si-free. Whether HSNL are present at the corundum-quartz grain boundaries cannot be determined with the methods used.

The features observed in this series of experiments indicate a transient nature of the HSNL inside corundum. With increasing temperature and experimental duration, HSNL bearing corundum seems to recrystallize, merge with neighboring individuals, and anneal the nanometer-sized phase resulting in larger, granular corundum grains with multiple sub-grains and inclusions of quartz and aqueous fluid (Fig. 5a*–c*).

Discussion

The role of aqueous fluid

Natural occurrences of corundum and quartz in direct contact without any reaction to Al_2SiO_5 are rare and generally interpreted to be a metastable feature preserved in fluid-free metamorphic rocks (Kihle et al. 2010; Kato et al. 2011). The absence of the reaction to Al_2SiO_5 is usually interpreted to be caused by low reaction kinetics due to a lack of a catalyzing fluid phase. However, we know of at least two natural examples contradicting this argument, which bear resemblance to the corundum–quartz assemblage of this and other fluid-bearing experimental studies (Fig. 1). One is a hydrothermally altered volcanic rock from Tasmania, in which a metastable corundum–quartz assemblage resulted from argillic overprint at moderate temperature and low pressure (Bottrill 1998). The second stems from a recent fluid inclusion study in garnets from the Athabasca granulite terrane in Canada, where corundum and quartz appear in mutual contact and together with pyrophyllite and carbonates as a

result of retrograde reequilibration of the trapped CO_2-rich fluids with the host mineral (Tacchetto et al. 2019; Carvalho et al. 2020).

Our results show that the presence of fluid does not necessarily promote the reaction of $Al_2O_3 + SiO_2 \rightarrow Al_2SiO_5$. Instead, fluid promotes the formation of nanolayers containing Si and OH (HSNL) inside and on the surface of the synthesized corundum plates. HRTEM images of the HSNL suggest that their structure resembles isolated Si-tetrahedral layers attached to Al-octahedral layers along $(0001)_{Crn}$ similar to dioctahedral phyllosilicates, e.g. kaolinite or pyrophyllite (Fig. 4b, c, e, compare HRTEM structures in pyrophyllite in Kogure et al. 2006). The octahedral layer in corundum is not identical to the octahedral layer in dioctahedral phyllosilicates regarding the position of Al ions in $(0001)_{Crn}$ and, e.g. $(001)_{Prl}$, respectively (Lee and Guggenheim 1981; Lewis et al. 1982). However, the connecting basal layer of Al octahedra is very likely modified in contact with the tetrahedral layer. Eng et al. (2000) reported a displacement of the Al ions in the surface layer of hydrated (0001) corundum crystal faces towards the position the Al ions hold in boehmite. A similar approximation of the corundum basal plane to the octahedral layer in dioctahedral phyllosilicates can be expected in contact with a silica layer. Due to the structural analogy to phyllosilicates and the comparison of the thickness of the HSNLs with the undisturbed surrounding corundum lattice in HRTEM images (Fig. 4b), it seems most likely that the HSNL are formed by silicon-tetrahedral layers substituting two Al-octahedral layers (double): $2Al^{3+} \rightarrow Si^{4+} + 2H^+$ or three Al-octahedral layers (triple): $3Al^{3+} \rightarrow 2Si^{4+} + H^+$ in corundum (Fig. 4e). The small size and lack of three-dimensional long-range order prohibits a more precise and definite characterization of the HSNL. However, the incorporation of H^+ in the nanolayers indicates that the presence of water in the experiments favors the formation of HSNL over the nucleation of the thermodynamically stable Al_2SiO_5 polymorphs rather than promoting the reaction towards the latter.

The dehydration of pyrophyllite (run 8) was expected to generate sillimanite and quartz at the chosen *P*–*T* conditions (Table 1). Instead, the experiment produced large volumes of mildly to strongly Si-enriched 2:3 mullite (Online Resource 1), the latter of which could be chemically classified as sillimullite according to Fischer et al. (2015). Mullites synthesized in run 8 are chemically closely related to naturally occurring mullite and much less similar to often nearly stochiometric synthetic 3:2 mullite produced in other (usually fluid free) experimental setups (Lenz et al. 2019). The possibility of a solid solution between mullite and sillimanite (Hariya et al. 1969) and the potential re-equilibration of mullite to sillimanite in long experiments (Brearley and Rubie 1990) is part of an ongoing debate, but could not be further constrained in the present study. It is, however, possible that the presence of fluid liberated by the pyrophyllite breakdown in our experiment facilitates the gradual incorporation of Si into metastable mullite from its quartz-saturated environment and hence supports the transformation into sillimullite and eventually stable sillimanite. If this was the case, the presence of aqueous fluid can be catalyzing one reaction towards equilibrium state in the ASH system, that of mullite + quartz → sillimanite*, while at the same time inhibiting the reaction corundum + quartz → sillimanite* (*or other aluminum–silicate polymorphs).

The influence of HSNL on reactions in the system ASH

The HSNL prevent adjacent, identically oriented corundum plates from coalescing and forming a single crystal, an observation that indicates that the nanolayers are the cause of growth obstruction along [0001]. Suchanek and Garcés (2010) reported the formation of "corundum nanosheets" (plate shaped corundum with large basal plane) from boehmite dehydration, with additional 1–10 wt% of silica, in hydrothermal experiments at ≤ 450 °C; 10 MPa. In the absence of silica, the corundum crystals developed a granular shape. Furthermore, X-ray photoelectron spectroscopy conducted on the (0001) surface of the corundum sheets and 6 nm below the surface showed the highest intensities for Si-derived bands (both Si2*p* and Si2*s*) at the surface (Suchanek and Garcés 2010). Silica-bearing features inside the corundum sheets were not reported.

For corundum plates with a surface predominantly consisting of HSNL-covered basal pinacoids, the interaction with adjacent quartz is very likely obstructed. Nanometer-sized minerals theoretically have a higher relative surface energy (or zeta potential) than their bulk minerals due to a large ratio of surface area/volume and should react more rapidly than the bulk minerals (Madden et al. 2006). Thin corundum plates adjacent to quartz should, therefore, react faster to Al_2SiO_5 polymorphs than larger corundum grains with smaller surface area/volume ratio. However, the HSNL on corundum may reduce the chemical potential gradient between the corundum and neighboring quartz drastically, thus acting as a thermodynamic barrier and preventing the two phases from reacting. Fisher et al. (2001) showed that the zeta potential difference of pure quartz and pure corundum in solution is about 85 mV at neutral pH. The addition of 2.7 vol% of silica to a corundum suspension decreased the zeta potential of corundum drastically and reduced the zeta potential difference of quartz and corundum to about 25 mV due to the adsorption of nano-silica particles (85 nm size) to the corundum surface. Similarly, the surface reactivity of corundum plates in contact with quartz or silica-saturated fluid with respect to quartz is probably reduced due to the HSNL covered surface. A minimized surface energy

also results in a smaller critical nucleus-size of corundum plates, which supports the survival of newly formed corundum plates so that they grow and increase in size. Furthermore, the zeta potential of silica becomes less negative with decreasing nanoparticle size (Diedrich et al. 2012), which could explain why the HSNL itself does not react with the corundum to form aluminum silicate. The experiments presented in this study do not grant direct insight into the moment of nucleation during the experiments; however, the nanostructures provide some clues about potential structural motifs of the nuclei. Because these nanostructures (HSNL) contain octahedral and tetrahedral layers similar to pyrophyllite, it seems plausible that within the given *P–T* range of the experiments discussed here the molecular structures of Al and Si in the aqueous solution favor an arrangement of such layers rather than octahedral chains and isolated tetrahedra as necessary to form Al_2SiO_5 polymorphs. It is known that pre-nucleation molecular structures can differ significantly from thermodynamically stable bulk phases in other systems, e.g. calcium carbonates and calcium phosphates (e.g. Lin and Chiu 2017). Direct observation of the pre-nucleation structures and the nucleation process itself is currently not possible due to experimental limitations. Quantum chemical modeling may provide more detailed insight into the nucleation process in the future.

Within the corundum plate rims grown on corundum single crystals, we measured a chemical profile for Si, which displayed a maximum concentration at the contact between single crystal and corundum plates followed by gradually decreasing Si content along the plate rim with increasing distance to the single crystal (Fig. 3). In contrast to this ramp-like Si profile, the Fe distribution along the contact between rim and single crystal resembles a normal diffusion profile (Fig. 3b, c). This could indicate independent diffusion mechanisms for Si and Fe along the corundum plate rim. Assuming a chemical gradient between corundum single crystals and quartz-saturated environment results in diffusive exchange of Si (and Al) ions through the corundum plate rim, the shape of the Si profile may be the result of fluid-mediated Si influx from the matrix along the HSNLs inside the corundum plates as well as along HSNL-bearing grain boundaries between the plates in the rim. The HSNL provides an ideal and fast pathway for Si diffusion along the basal plane $(0001)_{Crn}$ due to the shielding effect of the Si-tetrahedral layer in the HSNL, which allows for a Si mobility through the plate rims that is not stalled by interactions of free Si with the corundum plates. As a result of this particular diffusion along the HSNLs, the Si concentration could disproportionately increase at the single crystal plate rim as observed in Fig. 3b, c. The Si concentration profile could also reflect a specific growth phenomenon with elevated Si concentration at the plate rim–single crystal contact. However, if simple overgrowth alone was responsible for the peculiar Si profile, then the Fe profile should look similar and not like a diffusion profile.

The transient nature of the HSNL

Our series of experiments with diaspore starting material showed that at temperatures of 800 °C and prolonged run duration (> 2 weeks) the corundum habit changes significantly and HSNL disappear (Figs. 1d, f and 5c). Sub-µm-wide platy corundum produced at 550 °C gives way to µm-wide corundum plates with quartz inclusions at > 600 °C and finally to anhedral, granular corundum with elongated, round quartz inclusions (Fig. 5a–c). We interpret these findings as a gradual Ostwald ripening of the corundum and the HSNL included in corundum with increasing temperature and experiment duration (Fig. 5a*–c*). The HSNL are defects in the corundum structure that disintegrate during annealing when they become increasingly unstable at higher temperatures (compare Reich et al. 2006). Silica and OH, formerly included in the HSNL, accumulate within the corundum as round, often elongated quartz + aqueous fluid inclusions (Fig. 1f). The fluid inclusions are connected to a network of dislocation lines in granular corundum. The annealing eventually also enables neighboring plates to intergrow in [0001] and form larger crystals that show likewise curved phase boundaries towards surrounding quartz, thus indicating migrating interfaces (Figs. 1f and 5c*). Nearly spherical phase boundaries reduce the surface area between quartz and annealed corundum and thus minimize the surface energy between the two phases, which may contribute to preservation of the metastable coexistence at higher temperatures (see Figs. 1d and 5c, c*).

The features presented in this study are only directly visible and conclusively identifiable with TEM in oriented corundum (basal plane ‖ to the incident beam). The layers tend to disappear in experiments with longer runtimes (Figs. 1d, f and 5), all of which likely contributes to the HSNL having been overlooked until now. Furthermore, since Si is not an expected trace element in corundum, analyses (EMP or LA-ICPMS) of corundum usually do not include Si (Harlow and Bender 2013). However, the crystal shape of synthesized corundum, as well as µm to sub-µm sized quartz inclusions, give hints as to whether HSNLs might be, or have been, present in the grains and should be considered when interpreting experimental and natural findings (e.g. Guiraud et al. 1996; Kihle et al. 2010; Karmakar and Schenk 2015). Although the amount of silica in and on the corundum plates is small, its influence on the equilibration of the bulk phases in the system ASH can be critical, which needs to be taken into account, especially if corundum is interpreted to be an equilibrium feature and used for quantitative estimates (Manning 2007).

The impact of nano-particles or nano-minerals not only on environmental and biological processes (Waychunas et al. 2005; Hochella 2008; Wang 2014) but also on ore-forming processes (Reich et al. 2006, 2009) and extraterrestrial materials (Navrotsky et al. 2008; Dai et al. 2010) is fairly well known. In contrast, only little has been reported on the occurrence of nanophases in magmatic (Reich et al. 2009) and in metamorphic rocks (Wu et al. 2002), which presumably results from faster reaction kinetics and/or long reaction timescales leading to the resorption of nanophases in these settings prior to eruption or exhumation. Specifically for metamorphic systems, it, therefore, seems particularly useful to combine natural findings with experiments that might preserve temporally transient but process-controlling nanometer-sized phases.

Conclusion

After countless experiments in the ASH system Aramaki and Roy (1963, p. 1342) wrote: "It can easily be seen from the data that no structural prejudice is involved in the formation of quartz + corundum. Indeed, this is the strongest argument (in the absence of data) for the thermodynamic stability of this assemblage." Now, several decades later we can show that there is in fact a structural parameter that likely favors the growth of corundum and quartz that is not part of the crystal structure of the bulk phases. The presence of HSNL in and on corundum, formed together with quartz well inside the stability fields of Al_2SiO_5 polymorphs provides a possible explanation for the persistent metastability of the two bulk phases. Influencing both growth and dissolution behavior of corundum, the HSNL obviously stabilize corundum next to quartz due to the fact that the interface between the bulk phases is reduced to a minimum and both quartz and corundum are in contact with the HSNL but not with each other. Consequently, the reaction to Al_2SiO_5 polymorphs is inhibited. The extended metastability of quartz and corundum and suppression of Al_2SiO_5 polymorph formation is thus, not simply a problem of reaction kinetics but rather one of a temporally transient, thermodynamic barrier that is usually overlooked. Nanometer-sized phases are known to influence various geological systems and control mineral phase stability and geochemical reaction kinetics due to physicochemical properties, which can be drastically different from the respective macroscale phases (Hochella 2008, Wang 2014). The influence on processes in the ASH system of the nanometer-sized phase presented in this study should, therefore, be considered in both experimental and natural studies.

Thermodynamic modeling of metamorphic processes usually assumes bulk thermodynamic equilibration of a system. In this context, reaction pathways and the initial mineralogical composition of the system do not matter, but only the bulk chemistry and target state variables. Our findings show that this approach, while useful for understanding many metamorphic processes, can be insufficient under certain circumstances because it ignores the properties of the interface and grain boundary region, which link the thermodynamic properties of mineral phases to their grain size and shape. When natural or experimental observations seem to defy thermodynamics by showing unexpected metastability, kinetic hindrance is often invoked as the "obvious" explanation for the discrepancy, without direct evidence. However, as we have demonstrated, thermodynamic properties of hidden phases on mineral interfaces may be a critical factor controlling the reaction process. If these are considered, reaction pathways and the initial state of a system do matter. Research into the evidence for the formation of such phases has only started. Although understanding of reaction pathways is only in its infancy, it provides deeper insights into the conditions and dynamics of rock-forming processes in a given chemical system.

Supplementary Information The online version contains supplementary material available at https://doi.org/10.1007/s00410-021-01786-5.

Acknowledgements Special thanks to Anja Schreiber (GFZ Potsdam), Iryna Driehorst and Jörg Nissen (ZELMI at Technische Universität Berlin) for their support.

Author contributions According to CRediT (Contributor Roles Taxonomy) author statement:

DS investigation, conceptualization, methodology, writing—original draft preparation, visualization. RW investigation, visualization, data curation, writing—reviewing and editing. BW investigation, resources, writing- reviewing and editing. AL writing—reviewing and editing. MW writing- reviewing and editing. GF supervision, funding acquisition, writing—reviewing and editing.

Funding This work was supported by the Deutsche Forschungsgemeinschaft in the research group FOR 741 "Nanoscale Processes and Geomaterials Properties" [Grant No. FR 557/26].

Data availability statement All data and material used and discussed in the text are included as Figures and Tables in the main text or in the Electronic Supplementary Material.

Code availability Perplex_X (Connolly 2009, see References) was used to calculating and illustrate Fig. 1a.

Declarations

Conflict of interest The authors declare that they have no known competing financial interests or personal relationships that could have appeared to influence the work reported in this paper.

References

Althaus E (1966) Die bildung von pyrophyllit und andalusit zwischen 2000 und 7000 Bar H_2O-Druck. Naturwissenschaften 53:105–106

Aramaki S, Roy R (1962) Revised phase diagram for the system Al_2O_3–SiO_2. J Am Ceram Soc 45:229–242

Aramaki S, Roy R (1963) A new polymorph of Al_2SiO_5 and further studies in the system Al_2O_3–SiO_2–H_2O. Am Miner 48:1322–1347

Beitter T, Wagner T, Markl G (2008) Formation of kyanite-quartz veins of the Alpe Sponda, Central Alps, Switzerland: implications for Al transport during regional metamorphism. Contrib Miner Petrol 156:689–707. https://doi.org/10.1007/s00410-008-0310-4

Bratton RJ, Brindley GW (1962) Structure-controlled reactions in kaolinite—diaspore-boehmite clays. J Am Ceram Soc 45:1689–1699. https://doi.org/10.1111/j.1151-2916.1962.tb11048.x

Brearley AJ, Rubie DC (1990) Effects of H_2O on the disequilibrium breakdown of muscovite + quartz. J Petrol 31:925–956. https://doi.org/10.1093/petrology/31.4.925

Bottrill RS (1998) A corundum-quartz assemblage in altered volcanic rocks, bond range, Tasmania. Min Mag 62:325–332. https://doi.org/10.1180/002646198547710

Carr M, Fyfe WS (1960) Synthesis fields of some aluminium silicates. Geochim Cosmochim Acta 21:99–109. https://doi.org/10.1016/S0016-7037(60)80005-1

Carvalho BB, Bartoli O, Cesare B, Tacchetto T, Gianola O, Ferri F, Aradi LE, Szabó C (2020) Primary CO_2-bearing fluid inclusions in granulitic garnet usually do not survive. Earth Planet Sci Lett 536:116170. https://doi.org/10.1016/j.epsl.2020.116170

Clark SPJ, Robertson EC, Birch F (1957) Experimental determination of kyanite-sillimanite equilibrium relations at high temperatures and pressures. Am J Sci 255:628–640. https://doi.org/10.2475/ajs.255.9.628

Connolly JAD (2009) The geodynamic equation of state: what and how. Geochem Geophys Geosyst 10:1–19. https://doi.org/10.1029/2009GC002540

Dai ZR, Bradley JP, Joswiak DJ (2010) Possible in situ formation of meteoritic nanodiamonds in the early solar system. Nature 418:157–159. https://doi.org/10.1038/nature00897.1

Day HW (1973) The high temperature stability of muscovite plus quartz. Am Miner 58:255–262

DeVries RC (1964) The system Al_2SiO_5 at high temperatures and pressures. J Am Ceram Soc 47:230–237. https://doi.org/10.1111/j.1151-2916.1964.tb14401.x

Diedrich T, Dybowska A, Schott J, Valsami-Jones E, Oelkers EH (2012) The dissolution rates of SiO_2 nanoparticles as a function of particle size. Environ Sci Tech 46:4909–4915. https://doi.org/10.1021/es2045053

Eng PJ, Trainor TP, Brown GEJ, Waychunas GA (2000) Structure of the hydrated α-Al_2O_3 (0001) surface. Science 288:1029–1033. https://doi.org/10.1126/science.288.5468.1029

Fisher ML, Colic M, Rao MP, Lange FF (2001) Effect of silica nanoparticle size on the stability of alumina/silica suspensions. J Am Ceram Soc 84:713–718. https://doi.org/10.1111/j.1151-2916.2001.tb00731.x

Fischer RX, Tikhonova V, Birkenstock J, Fischer LA, Herrmann K, Mengel K, Schneider H (2015) A new mineral from the Bellerberg, Eifel, Germany, intermediate between mullite and sillimanite. Am Miner 100:1493–1501. https://doi.org/10.2138/am-2015-4966

Giardini AA, Kohn JA, Eckart DW, Tydings JE (1961) The formation of coesite and kyanite from pyrophyllite at very high pressures and high temperatures. Am Miner 46:976–982

Grapes R (2011) Experimental breakdown of staurolite + inclusions of albite and muscovite at 800 °C and 0.1 GPa. Miner Mag 75:117–133. https://doi.org/10.1180/minmag.2011.075.1.117

Guiraud M, Kienast JR, Ouzegane K (1996) Corundum-quartz bearing assemblage in the Ihouhaounene area (In Ouzzal, Algeria). J Metamorph Geol 14:754–762. https://doi.org/10.1111/j.1525-1314.1996.00046.x

Hariya Y, Dollase WA, Kennedy GC (1969) An experimental investigation of the relationship of mulite to sillimanite. Am Miner 54:1419–1441

Harlov DE, Milke R (2002) Stability of corundum + quartz relative to kyanite and sillimanite at high temperature and pressure. Am Miner 87:424–432. https://doi.org/10.2138/am-2002-0406

Harlov DE, Milke R, Gottschalk M (2008) Metastability of sillimanite relative to corundum and quartz in the kyanite stability field: competition between stable and metastable reactions. Am Miner 93:608–617. https://doi.org/10.2138/am.2008.2655

Harlow GE, Bender W (2013) A study of ruby (corundum) compositions from the Mogok Belt, Myanmar: searching for chemical fingerprints. Am Miner 98:1120–1132. https://doi.org/10.2138/am.2013.4388

Hochella MFJ (2008) Nanogeoscience: from origins to cutting-edge applications. Elements 4:373–380. https://doi.org/10.2113/gselements.4.6.373

Holland TJB, Powell R (2011) An improved and extended internally consistent thermodynamic dataset for phases of petrological interest, involving a new equation of state for solids. J Metamorph Geol 29:333–383. https://doi.org/10.1111/j.1525-1314.2010.00923.x

Holdaway MJ (1971) Stability of andalusite and the aluminosilicate phase diagram. Am J Sci 271:97-l3l. https://doi.org/10.2475/ajs.271.2.97

Huang WL, Wyllie PJ (1974) Melting relations of muscovite with quartz and sanidine in the K_2O–Al_2O_3–SiO_2–H_2O system to 30 kilobars and an outline of paragonite melting relations. Am J Sci 274:378–395. https://doi.org/10.2475/ajs.274.4.378

Karmakar S, Schenk V (2015) Neoarchean UHT metamorphism and paleoproterozoic UHT reworking at Uweinat in the East Sahara Ghost Craton, SW Egypt: Evidence from petrology and texturally controlled in situ monazite dating. J Petrol 56:1703–1742. https://doi.org/10.1093/petrology/egv051

Kato M, Hiroi Y, Harlov DE, Satish-Kumar M, Hokada T (2011) Metastable corundum + quartz + andalusite association in pelitic granulite from the Kerala Khondalite Belt, southern India. J Miner Petrol Sci 106:195–203. https://doi.org/10.2465/jmps.101116

Kerrick DM (1990) The Al_2SiO_5 polymorphs: reviews in mineralogy. De Gruyter, Berlin

Kihle J, Harlov DE, Frigaard O, Jamtveit B (2010) Epitaxial quartz inclusions in corundum from a sapphirine-garnet boudin, Bamble Sector, SE Norway: SiO_2–Al_2O_3 miscibility at high P–T dry granulite facies conditions. J Metamorph Geol 28:769–784. https://doi.org/10.1111/j.1525-1314.2010.00891.x

Kogure T, JIge M, Kameda J, Yamagishi A, Miyawaki R, Kitagawa R (2006) Stacking structures in pyrophyllite revealed by high-resolution transmission electron microscopy (HRTEM). Am Miner 91:1293–1299. https://doi.org/10.2138/am.2006.1997

Lee JH, Guggenheim S (1981) Single crystal X-ray refinement of pyrophyllite-1Tc. Am Miner 66:350–357

Lenz S, Birkenstock J, Fischer LA, Schüller W, Schneider H, Fischer RX (2019) Natural mullites: chemical composition, crystal structure, and optical properties. Eur J Miner 31:353–367. https://doi.org/10.1127/ejm/2019/0031-2812

Lewis J, Schwarzenbach D, Flack HD (1982) Electric field gradients and charge density in corundum, α-Al_2O_3. Acta Crystallogr Sect A 38:733–739. https://doi.org/10.1107/S0567739482001478

Lin T, Chiu C (2017) Structures and infrared spectra of calcium phosphate clusters by Ab initio methods with implicit solvation models. Phys Chem Chem Phys. https://doi.org/10.1039/C7CP05975B

Madden AS, Hochella MFJ, Luxton TP (2006) Insights for size-dependent reactivity of hematite nanomineral surfaces through Cu^{+2} sorption. Geochim Cosmochim Acta 70:4095–4104. https://doi.org/10.1016/j.gca.2006.06.1366

Manning CE (2007) Solubility of corundum + kyanite in H_2O at 700°C and 10 kbar: evidence for Al–Si complexing at high pressure and temperature. Geofluids 7:258–269. https://doi.org/10.1111/j.1468-8123.2007.00179.x

Momma K, Izumi F (2011) VESTA 3 for three-dimensional visualization of crystal, volumetric and morphology data. J Appl Crystallogr 44:1272–1276. https://doi.org/10.1107/S0021889811038970

Navrotsky A, Mazeina L, Majzlan J (2008) Size-driven structural and thermodynamic complexity in iron oxides. Science 319:1635–1638. https://doi.org/10.1126/science.1148614

Pattison DRM (1992) Stability of andalusite and sillimanite and the Al_2SiO_5 triple point: constraints from the Ballachulish aureole. Scotl J Geol 100:423–446. https://doi.org/10.1086/629596

Reich M, Satoshi U, Kesler SE, Wang L (2006) Thermal behavior of metal nanoparticles in geologic materials. Geology 34:1033–1036. https://doi.org/10.1130/G22829A.1

Reich M, Zúñiga A, Amigo Á, Vargas G, Morata D, Palacios C, Parada MÁ, Garreaud RD (2009) Formation of cristobalite nanofibers during explosive volcanic eruptions. Geology 37:435–438. https://doi.org/10.1130/G25457A.1

Rudnick RL, Gao S (2003) The composition of the continental crust. In: Rudnick RL, Holland HD, Turekian KK (eds) The crust, treatise on geochemistry. Elsevier-Pergamon, Oxford, pp 1–64

Saalfeld H, Junge W (1983) Thermal decomposition of kyanite single crystals. Tscherm Miner Petrogr Mitt 26:17–26. https://doi.org/10.1007/BF01084758

Schilling F, Wunder B (2004) Temperature distribution in piston-cylinder assemblies: numerical simulations and laboratory experiments. Eur J Miner 16:7–14. https://doi.org/10.1127/0935-1221/2004/0016-0007

Schneider H, Komarneni S (2005) Foreign cation incorporation in mullite. Wiley VCH, Weinheim

Suchanek WL, Garcés JM (2010) Hydrothermal synthesis of novel alpha alumina nano-materials with controlled morphologies and high thermal stabilities. CrystEngComm. https://doi.org/10.1039/B927192A

Tacchetto T, Bartoli O, Cesare B, Berkesi M, Aradi LE, Dumond G, Szabó C (2019) Multiphase inclusions in peritectic garnet from granulites of the Athabasca granulite terrane (Canada): evidence of carbon recycling during Neoarchean crustal melting. Chem Geol 508:197–209. https://doi.org/10.1016/j.chemgeo.2018.05.043

Wahl FM, Grim RE, Graf RB (1961) Phase transformation in silica–alumina mixtures as examined by continous X-ray diffraction. Am Miner 46:1064–1076

Wang Y (2014) Nanogeochemistry: nanostructures, emergent properties and their control on geochemical reactions and mass transfers. Chem Geol 378–379:1–23. https://doi.org/10.1016/j.chemgeo.2014.04.007

Waychunas GA, Kim CS, Banfield JF (2005) Nanoparticulate iron oxide minerals in soils and sediments: unique properties and contaminant scavenging mechanisms. J Nanopart Res 7:409–433. https://doi.org/10.1007/s11051-005-6931-x

Whitney DL, Evans BW (2010) Abbreviations for names of rock-forming minerals. Am Miner 95:185–187. https://doi.org/10.2138/am.2010.3371

Wirth R, Wunder B (2000) Characterization of OH– containing phases by TEM using electron energy-loss spectroscopy (EELS): clinohumite–OH, chondrodite–OH, phase A and the (F, OH)-solid solution series of topaz. J Trace Microprobe Tech 18:35–49

Wu X, Han Y, Meng D, Li D (2002) Discovery and implication of $P2_1/n$ crystal structure on a nano-scale in single jadeite crystals. Earth Planet Sci Lett 197:165–169. https://doi.org/10.1016/S0012-821X(02)00476-4